Precomputed Acceleration Noise for Improved Rigid-Body Sound

Jeffrey N. Chadwick   Changxi Zheng   Doug L. James

Cornell University

Figure 1: *Our model efficiently synthesizes acceleration noise due to rigid-body collisions in a variety of multibody collision scenarios.*

Abstract

We introduce an efficient method for synthesizing acceleration noise – sound produced when an object experiences abrupt rigid-body acceleration due to collisions or other contact events. We approach this in two main steps. First, we estimate continuous contact force profiles from rigid-body impulses using a simple model based on Hertz contact theory. Next, we compute solutions to the acoustic wave equation due to short acceleration pulses in each rigid-body degree of freedom. We introduce an efficient representation for these solutions – *Precomputed Acceleration Noise* – which allows us to accurately estimate sound due to arbitrary rigid-body accelerations. We find that the addition of acceleration noise significantly complements the standard modal sound algorithm, especially for small objects.

CR Categories: I.3.5 [Computer Graphics]: Computational Geometry and Object Modeling—Physically based modeling; I.6.8 [Simulation and Modeling]: Types of Simulation—Animation; H.5.5 [Information Systems]: Information Interfaces and Presentation—Sound and Music Computing

Keywords: Sound synthesis, acceleration noise, contact sounds, modal analysis

Links: ◈ DL 📄 PDF 🌐 WEB

1 Introduction

The rattling of coins dropped on a table, the jingling of a set of car keys and the cascade of noise from a shattering pane of glass are all familiar sound phenomena. Simulation of rigid-body dynamics for scenarios such as these is a widely studied field in the computer animation community. Physically based rigid-body solvers are capable of producing detailed visual behavior virtually indistinguishable from reality. The linear modal sound model is the most popular approach for resolving the sound of colliding rigid bodies in computer animation and virtual environments [van den Doel et al.

2001; O'Brien et al. 2002; Bonneel et al. 2008]. This method efficiently and accurately captures the collision-induced ringing noise produced by a wide variety of objects. Numerous methods for evaluating *acoustic transfer* functions – solutions to the Helmholtz equation characterizing how vibrating objects produce sound – have been combined with modal sound algorithms to produce more realistic results (e.g., [James et al. 2006]).

In spite of these advances, numerous rigid-body collision scenarios exist for which current sound models produce unconvincing results. Rigid-body impacts produce sound primarily due to two sources: "ringing noise" [Richards et al. 1979b] and "acceleration noise" [Richards et al. 1979a]. Ringing noise refers to sound due to object vibrations. Acceleration noise, on the other hand, is produced when objects undergo large rigid-body accelerations. If a body experiences acceleration over a sufficiently short time scale, the resulting pressure disturbance in the surrounding medium is perceived as sound.

While current rigid-body sound models synthesize convincing ringing noise, no efficient models exist for synthesizing sound due to acceleration noise. Consequently, synthesized rigid-body impact sounds tend to have an incorrect initial attack and lack the "crispness" characteristic of real impact

Figure 2: *Small ball bearings vibrate too quickly to produce audible modal sound. Instead, their sound is the result of rigid acceleration experienced during collisions.*

sounds. In fact, for small objects that only vibrate at frequencies beyond the range of human hearing (small ball bearings, dice, etc.), current approaches produce no sound whatsoever. While this omission is obvious even for certain single-object collision sounds, it is particularly noticeable in scenes involving large ensembles of small colliding objects. Prior work on modal sound synthesis has modeled transient contact sounds based on recorded audio [van den Doel et al. 2001; Lloyd et al. 2011; Zheng and James 2011]. Different approaches for improving contact modeling in modal sound synthesis have been studied in [Ren et al. 2010] and [Zheng and James 2011], but these methods still omit transient acceleration noise. Verma and Meng [2000] introduced transient-modeling synthesis (TMS), which extends earlier work on spectral modeling synthesis [Serra and Smith 1990]. TMS provides a general system for decomposition and synthesis of audio signals involving both sinusoidal (modal) and transient components; however, it does not provide a physics-based approach for synthesizing sounds from arbitrary rigid objects.

To address this limitation, we propose a simple and efficient model for acceleration noise which can be easily integrated with exist-

ing rigid-body sound pipelines. Resolving acceleration noise for a rigid-body simulation is accomplished via two main steps:

1. *Contact force estimation*: Rigid-body solvers separate colliding objects by applying repulsive impulses to produce instantaneous velocity changes in the colliding objects. We use Hertz contact theory [Hertz 1882; Johnson 1985] to estimate physically plausible continuous rigid-body acceleration profiles from each collision impulse.

2. *Acoustic radiation*: We present an efficient precomputed representation for sound due to objects undergoing short acceleration pulses. This allows us to reconstruct arbitrary acceleration noise signals from an object, while avoiding impractical audio-rate time stepping of the acoustic wave equation.

Other Related Work: Previous work on acceleration noise has been motivated by noise control requirements in industrial settings. Koss and Alfredson [1973] investigated the transient sound radiated by colliding spheres and found that a contact model based on Hertzian impact theory could be used to approximately recover pressure waveforms measured in experiments. Other studies have investigated acceleration noise due to colliding spheres [Richards et al. 1979a; Richards et al. 1979b] and other simple geometries [Endo et al. 1981; Yufang and Zhongfang 1992]. Acceleration noise for impacted plates has been studied experimentally by Wåhlin et al. [1994] and Chaigne & Lambourg [2001]. Numerical models for plate acceleration noise have been investigated by Shedin et al. [1999] using experimentally recorded impact forces, and by Lambourg et al. [2001] and Ross & Ostiguy [2007] using Hertz-like impact forces. These numerical approaches have shown good agreement with experimental results; however, they use expensive finite element or finite difference discretizations to simulate dynamics, making them undesirable for animation sound purposes.

In principle, both ringing noise and acceleration noise can be resolved simultaneously by explicitly solving for a body's surface motion using standard numerical approaches such as the finite element method. The effect of an object's surface motion can be propagated to the listener by solving the time-domain wave equation in the region surrounding the object (e.g., [Mehraby et al. 2011]). In O'Brien et al. [2001], the authors used explicit time-stepping of nonlinear elastic finite element meshes to resolve object surface deformations at audio time-stepping rates and computed sound by directly propagating surface velocities at each object triangle to the listener's location. While this method could in principle resolve detailed surface deformations sufficient for synthesizing both ringing and acceleration noise, rigid-body accelerations (and indeed high-frequency ringing noises) are the result of compression occurring over very small regions and time scales [Johnson 1985]. Accurately resolving these scales via finite element simulation requires spatial and temporal resolutions to be prohibitively high for computer animation purposes. Moreover, we find that rigid-body acceleration tends to produce complex time-varying pressure signals even for simple pulse-like velocity changes (see Figures 4, 5). Producing sound directly from an object's surface velocity fails to capture this wave radiation.

Hertz originally proposed a model for normal contact between elastic bodies based on a nonlinear spring force [1882]. This model can be used to determine the continuous contact forces acting on dynamically colliding bodies [Johnson 1985; Flores et al. 2008]. Analytical approximations of these time-dependent contact forces are also available for certain geometries. Hertz contact and other similar theories are used widely in the multibody systems community to predict continuous contact forces [Gilardi and Sharf 2002; Schiehlen and Seifried 2004; Flores et al. 2006; Flores et al. 2008; Flores et al. 2011]. In the context of sound synthesis, Hertz-like contact force models have been considered for excitation of modal vibration in the computer graphics community [van den Doel et al. 2001] and elsewhere [Stoelinga and Lutfi 2011].

2 Background

Given an object O, let Ω denote its exterior domain and $\delta\Omega$ denote its boundary. Acoustic pressure fluctuations in Ω are modeled via the acoustic wave equation

$$\frac{1}{c^2}\frac{\partial^2 p(\boldsymbol{x},t)}{\partial t^2} = \nabla^2 p(\boldsymbol{x},t), \quad \boldsymbol{x} \in \Omega \qquad (1)$$

where c is the speed of sound in the medium (343.2m/s in air at standard temperature and pressure). The effect of O's surface motion on p is introduced via the boundary condition

$$\nabla p(\boldsymbol{x},t) \cdot \mathbf{n}(\boldsymbol{x}) = -\rho a_n(\boldsymbol{x},t), \quad \boldsymbol{x} \in \delta\Omega, \qquad (2)$$

where ρ refers to density of the surrounding medium, assumed constant (1.2041kg/m^3 for air at standard pressure and 20° C). $\mathbf{n}(\boldsymbol{x})$ and $a_n(\boldsymbol{x},t)$ denote the surface normal and normal acceleration of position $\boldsymbol{x}$ on O's surface.

We may also express (1) as a pair of first-order partial differential equations (PDEs) describing acoustic pressure and particle velocity:

$$\frac{\partial p(\boldsymbol{x},t)}{\partial t} = -c^2 \rho \nabla \cdot \mathbf{v}(\boldsymbol{x},t) \qquad (3)$$

$$\frac{\partial \mathbf{v}(\boldsymbol{x},t)}{\partial t} = -\frac{1}{\rho}\nabla p(\boldsymbol{x},t) \qquad (4)$$

In this case, (2) and (4) imply that $\frac{\partial v_n}{\partial t} = a_n$ on $\delta\Omega$, where v_n is the normal particle velocity on the object's surface. The wave equation boundary condition (2) accounts for contributions from arbitrary surface motion, including rigid-body motion. Intuitively, when an object moves through the air, the velocity of the surrounding air must change to match that of the moving object at its surface. When an object undergoes an abrupt change in velocity, the resulting fluctuation in the surrounding air pressure is propagated according to the wave equation and interpreted by a listener as sound (see Figure 5).

Most prior approaches for synthesizing sound from vibrating objects have assumed that the visual motion of an object is governed entirely by rigid-body dynamics. Object deformations are assumed to be small and independent of an object's rigid-body behavior, and are modeled by simulating vibrations in small basis of linear mode shapes, transformed in to the object's rigid-body frame [O'Brien et al. 2002]. Under the assumption that rigid motion and modal vibration are independent, we may write the normal acceleration on an object's surface as $a_n(\boldsymbol{x},t) = a_n^R(\boldsymbol{x},t) + a_n^M(\boldsymbol{x},t)$ where a_n^R and a_n^M refer to normal surface acceleration due to rigid-body motion and modal vibration, respectively. By the linearity of (1) and (2), we can write the acoustic pressure as $p(\boldsymbol{x},t) = p^R(\boldsymbol{x},t) + p^M(\boldsymbol{x},t)$ where p^R and p^M are the pressure contributions due to rigid-body motion and modal surface vibration. Existing rigid-body sound models only compute p^M, neglecting the acceleration noise contribution p^R. This omission is particularly noticeable for small, hard objects such as plastic dice and steel ball bearings. The linear vibration modes for these objects vibrate at frequencies well above 20 kHz. Consequently, modal sound algorithms predict sound well beyond the frequency range of human hearing for these objects.

3 Contact Force Estimation

We run rigid-body simulations using a solver based on [Guendelman et al. 2003] in which collisions are resolved via *impulses*. Impulses are time-integrated forces that are treated as instantaneous changes in linear and angular momentum for the purpose of physics-based animation of rigid-body dynamics. When two objects collide, impulses are applied to ensure that the resulting velocity changes cause intersecting regions in the objects to separate. The method of instantaneously updating velocities to resolve contact is widely used in rigid-body animation and produces compelling visual results. Unfortunately, this approach does not provide a suitable continuous acceleration profile for use in (2). We could, in principle, acquire continuous acceleration data by resolving rigid-body contacts with a simple Kelvin-Voight penalty law (used previously for sound synthesis in, e.g., [Chadwick et al. 2009]). However, recovering physically plausible acceleration time scales would require both careful parameter tuning and simulation at very high rates.

Contact force modeling is a widely studied field [Johnson 1985; Flores et al. 2008] and numerous continuous contact force models are available. Methods have been developed to account for damping during contact events [Hunt and Crossley 1975], hysteresis [Lankarani and Nikravesh 1990] and arbitrary geometric structure in contact regions [Hippmann 2004]. Evaluating these contact force models in the context of dynamics simulation requires careful parameter tuning and potentially costly numerical simulation [Papetti et al. 2011]. The goal in this section is to present a simple and efficient model for estimating the continuous contact forces necessary to demonstrate rigid acceleration noise. Therefore, we appeal to a simple model based on the Hertz theory of elastic contact.

3.1 Hertz Contact Theory

Hertz contact theory states that the normal contact force between two colliding elastic bodies is given by

$$f = Kd^{1.5} \tag{5}$$

where d is the penetration depth at the contact point and K is a constant depending on the material properties and local contact geometry of the colliding bodies. For a collision between two frictionless spheres, $K = (4/3)\sqrt{r}E^*$ and the time dependence of the contact force for a collision beginning at time t_0 can be approximated by a half-sine pulse [Johnson 1985]

$$S(t; t_0, \tau) = \begin{cases} \sin\left(\frac{\pi(t-t_0)}{\tau}\right) & \text{if } t_0 \leq t \leq t_0 + \tau \\ 0 & \text{otherwise} \end{cases} \tag{6}$$

where τ is a time scale defined by

$$\tau = 2.87 \left(\frac{m^2}{rE^{*2}V}\right)^{1/5}. \tag{7}$$

V is the normal impact speed and the other constants used in (7) are defined as follows:

$$\frac{1}{r} = \frac{1}{r_1} + \frac{1}{r_2}, \quad \frac{1}{m} = \frac{1}{m_1} + \frac{1}{m_2}, \quad \frac{1}{E^*} = \frac{1-\nu_1^2}{E_1} + \frac{1-\nu_2^2}{E_2}. \tag{8}$$

R_i, m_i, ν_i and E_i are the radius, mass, Poisson ratio and Young's modulus for spheres $i = 1, 2$. Force profiles of the form (7) have been used to model continuous contact forces for acceleration noise due to simple geometries in [Koss and Alfredson 1973; Richards et al. 1979a; Endo et al. 1981; Yufang and Zhongfang 1992].

3.2 Contact Time Scale Estimation

Given a collision between objects O_1 and O_2, let $\boldsymbol{x}_1$ and $\boldsymbol{x}_2$ be the contact locations in the coordinate frames of O_1 and O_2 (see Figure 3(b)). We use (6-7) to estimate a time scale and time-dependent contact force for the collision. Let $\mathbf{n}_i$ be the contact impulse direction in O_i's coordinate frame. To leverage the analytical force profile (6-7) we locally approximate O_1 and O_2 with spheres in the vicinity of the contact points. We compute the discrete mean curvature $H_1(\boldsymbol{x}_1)$ of O_1 at $\boldsymbol{x}_1$ (similarly, $H_2(\boldsymbol{x}_2)$) [Meyer et al. 2002]. Next, we estimate proxy sphere radii as $r_1 = 1/H_1(\boldsymbol{x}_1)$ and $r_2 = 1/H_2(\boldsymbol{x}_2)$. If O_1 and O_2 are in fact spheres, then r_1 and r_2 recover their radii exactly up to mesh discretization error. We use r_1 and r_2 to compute the term $1/r$ from (8). The material parameter in (8) can be computed trivially using the material properties of O_1 and O_2. Finally, we require the effective mass term $1/m$. For object O_i, let

$$\frac{1}{m_i} = \frac{1}{M_i} + \mathbf{n}_i^T \mathbf{I}_{\boldsymbol{x}_i-\boldsymbol{x}_0^i}^T \mathbf{M}_i^{-1} \mathbf{I}_{\boldsymbol{x}_i-\boldsymbol{x}_0^i} \mathbf{n}_i. \tag{9}$$

That is, $1/m_i$ is the inverse effective mass experienced by a force acting on body O_i at position $\boldsymbol{x}_i$ in direction $\mathbf{n}_i$. M_i, $\boldsymbol{x}_0^i$ and $\mathbf{M}_i$ refer to the mass, center of mass and moment of inertia matrix in O_i's coordinate frame. For a vector $\mathbf{z} \in \mathbb{R}^3$, $\mathbf{I}_{\mathbf{z}}$ is the 3×3 cross product matrix defined by $\mathbf{I}_{\mathbf{z}}\mathbf{v} = \mathbf{z} \times \mathbf{v}, \forall \mathbf{v} \in \mathbb{R}^3$. The geometry used for this calculation is illustrated in Figure 3.

3.3 Acceleration Profile Estimation

Following the notation of §3.2, suppose that the impulses applied to some position on O_1 and O_2 are $\mathbf{j}$ and $-\mathbf{j}$ in world coordinates (see Figure 3(a)). Let $\boldsymbol{x}_1$, $\boldsymbol{x}_2$ and $\mathbf{j}_1, \mathbf{j}_2$ be the collision points and values of the impulse when transformed in to the respective coordinate frames of O_1 and O_2 and let $\widehat{\mathbf{j}}_i = \mathbf{j}_i / \|\mathbf{j}_i\|$. For an impulse $\mathbf{j}$ occurring at time t_0 and producing a force profile with time scale τ (§3.2), we choose a scaling factor γ so that the time integrated Hertz contact force matches the magnitude of the impulse:

$$\int_0^\infty \gamma S(t; t_0, \tau) dt = \|\mathbf{j}\|. \tag{10}$$

From (6) and (10) we see that $\gamma = \pi\|\mathbf{j}\|/2\tau$. Scaling by γ guarantees consistency with simulated rigid-body dynamics. Finally, we assume that the change in position/orientation of body O_i is negligible over the time period during which the contact force is applied. This assumption is reasonable given the short timescales associated with contact (τ is typically in the range of 10-100μs). Under this assumption, the translational and angular accelerations in O_i's coordinate frame are given by

$$\mathbf{a}_i(t) = \frac{\gamma}{M_i} \widehat{\mathbf{j}}_i S(t; t_0, \tau), \tag{11}$$

$$\boldsymbol{\alpha}_i(t) = \gamma \mathbf{M}^{-1} \left(\left(\boldsymbol{x}_i - \boldsymbol{x}_0^i\right) \times \widehat{\mathbf{j}}_i\right) S(t; t_0, \tau). \tag{12}$$

For an arbitrary rigid-body collision, we use (11-12) to determine continuous translational and rotational acceleration signals with time-dependence given by a half-sine pulse (6).

4 Precomputed Acceleration Noise

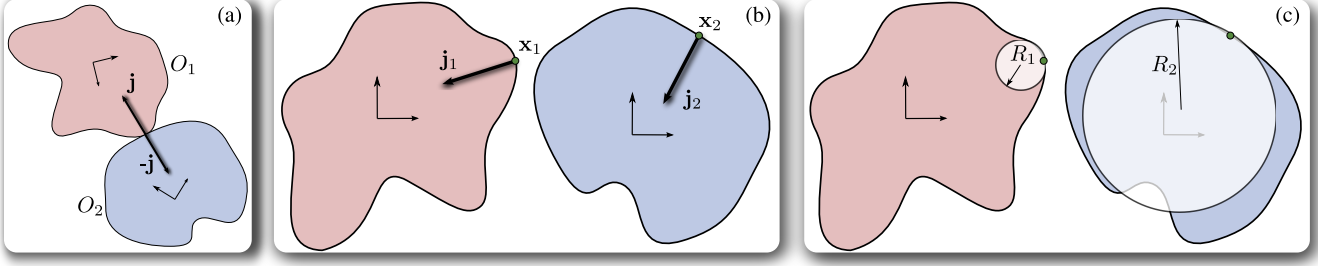In this section, we introduce an efficient method for synthesizing sound due to continuous rigid-body acceleration.

Figure 3: Contact Geometry: (a): *Two objects collide and experience equal and opposite impulses;* (b): *The impulses and contact positions and sound listening positions are transformed in to each object's rest frame.* (c): *We fit spheres whose curvatures match the curvatures at points $\boldsymbol{x}_1$ and $\boldsymbol{x}_2$ on O_1 and O_2. These proxy geometries are used to determine a Hertz impact time scale using (7).*
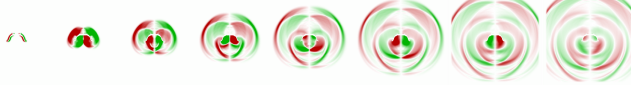

Figure 4: Rigid acceleration pressure: *Time evolution of the pressure field surrounding a bowl undergoing a short horizontal acceleration pulse. We precompute these rigid-body acceleration responses for sound synthesis.*

4.1 Directional Pressure Fields

Let $\mathbf{a}(t) = [a_1(t)\ a_2(t)\ a_3(t)]^T$, $\boldsymbol{\alpha}(t) = [\alpha_1(t)\ \alpha_2(t)\ \alpha_3(t)]^T$ and $\boldsymbol{x}_0$ refer to the translational acceleration, angular acceleration and center of mass position of a rigid body O at time t in O's coordinate frame. Normal rigid surface acceleration a_n^R at position $\boldsymbol{x}$ on O's surface can be written as

$$a_n^R(\boldsymbol{x}, t) = \mathbf{a}(t) \cdot \mathbf{n}(\boldsymbol{x}) + (\boldsymbol{\alpha}(t) \times (\boldsymbol{x} - \boldsymbol{x}_0)) \cdot \mathbf{n}(\boldsymbol{x})$$
$$= \sum_{i=1}^{3} a_i(t) \mathbf{e}_i \cdot \mathbf{n}(\boldsymbol{x}) + \sum_{i=1}^{3} \alpha_i(t) (\mathbf{e}_i \times (\boldsymbol{x} - \boldsymbol{x}_0)) \cdot \mathbf{n}(\boldsymbol{x})$$
(13)

where $\mathbf{e}_i \in \mathbb{R}^3$ is the vector with components $e_{ij} = \delta_{ij}$. We write rigid-body acceleration noise in O's coordinate frame as a sum of contributions from each of these acceleration components:

$$p(\boldsymbol{x}, t) = \sum_{i=1}^{3} p_{T,i}(\boldsymbol{x}, t) + \sum_{i=1}^{3} p_{R,i}(\boldsymbol{x}, t).$$
(14)

The components $p_{T,i}$ are contributions due to translational acceleration; solutions to (1) subject to

$$\nabla p_{T,i} \cdot \mathbf{n}(\boldsymbol{x}) = -\rho\, a_i(t)\, \mathbf{e}_i \cdot \mathbf{n}(\boldsymbol{x})$$
(15)

and $p_{R,i}$ are contributions due to rotational acceleration; that is, solutions to (1) subject to

$$\nabla p_{R,i} \cdot \mathbf{n}(\boldsymbol{x}) = -\rho\, \alpha_i(t) (\mathbf{e}_i \times (\boldsymbol{x} - \boldsymbol{x}_0)) \cdot \mathbf{n}(\boldsymbol{x}).$$
(16)

Figure 4 illustrates the time evolution of $p_{T,1}$ for a bowl undergoing a short acceleration pulse along its x-axis. Given a continuous rigid acceleration signal, we can solve (3-4) for each of the boundary conditions (15) and (16) independently and use (14) to recover the total acceleration noise. It is straightforward to time step (3-4) using a staggered grid finite difference discretization (e.g., [Liu and Tao 1997]). However, the cost of this approach makes it infeasible for animation sound synthesis.

4.2 Precomputed Acceleration Noise

Instead of directly solving (3-4) over the length of a rigid-body animation, we precompute solutions for short acceleration pulses in each of the 6 rigid-body degrees of freedom. We use these pulses to interpolate boundary conditions (15-16) and reconstruct acceleration sound due to arbitrary rigid-body acceleration.

For an object O we define a pulse time scale h and pulse function $\psi(t; h)$. We use a Mitchell-Netravali cubic filter [1988]

$$\psi(t; h) = \frac{1}{18} \begin{cases} -15y^3 + 18y^2 + 9y + 2 & |t| \leq h \\ 5(1+y)^3 - 3(1+y)^2 & h \leq |t| \leq 2h, \\ 0 & \text{otherwise,} \end{cases}$$
(17)

where $y \equiv 1 - |t|$. Let $p_{T,i}^{(h)}(\boldsymbol{x}, t)$ be the solution to (3-4) for $t \geq -2h$ subject to (15) with $a_i(t) = \psi(t; h)$. Rotational terms $p_{R,i}^{(h)}$ are defined similarly. Figure 5 illustrates the boundary condition (15) and resulting pressure time series $p_{T,1}^{(h)}(\boldsymbol{x}, t)$ at an exterior listening position. For arbitrary accelerations $a_i(t)$ and $\alpha_i(t)$ defined for $t \geq 0$, the directional pressure fields are approximated by

$$p_{T,i}(\boldsymbol{x}, t) \approx \sum_{k=0}^{\infty} a_i(kh)\, p_{T,i}^{(h)}(\boldsymbol{x}, t - kh),$$
(18)

$$p_{R,i}(\boldsymbol{x}, t) \approx \sum_{k=0}^{\infty} \alpha_i(kh)\, p_{R,i}^{(h)}(\boldsymbol{x}, t - kh).$$
(19)

which follows from the linearity of (3-4) and the approximation of boundary conditions (15-16) by basis functions $\psi(t; h)$.

The functions $p_{T,i}^h$ and $p_{R,i}^h$ discussed above represent the sounds produced by an object experiencing a short acceleration pulse in each of its six rigid-body degrees of freedom. Assuming that we
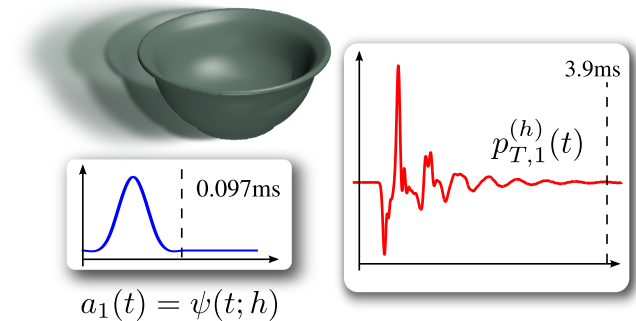

$$a_1(t) = \psi(t; h)$$

Figure 5: Precomputing directional pulses: *We accelerate the bowl along its x-axis with an acceleration profile given by $\psi(t; h)$. This acceleration produces the pressure fluctuations $p_{T,1}^{(h)}(t)$ at a listening position $\boldsymbol{x}$ exterior to the object. We observe that pressure fluctuations at $\boldsymbol{x}$ persist for much longer than the duration of $\psi(t; h)$ due to acoustic reflections inside the bowl.*

are able to compute these functions at arbitrary positions/times, (18) and (19) allow us to reconstruct sound due to arbitrary rigid-body accelerations (up to a temporal resolution determined by h). Unfortunately, computing $p_{T,i}^h$ and $p_{R,i}^h$ for every listening time and position required by an animation is impractical. Therefore, we introduce a data-driven representation for the fields $p_{T,i}^{(h)}$ and $p_{R,i}^{(h)}$ by discretizing the angular space surrounding an object and computing a radial series approximation of the pressure field in each direction. This representation is similar to the far-field acoustic transfer maps introduced in [Chadwick et al. 2009], in which the authors compute radial series approximations to solutions of the Helmholtz equation. However, their approach does not handle time-dependent solutions, and cannot be directly used here.

The remainder of this section details our representation for the functions $p_{T,i}^h$ and $p_{R,i}^h$. Since we apply identical methods to each of these 6 functions, we will omit subscripts and superscripts and refer to the function to be approximated simply as $p(\boldsymbol{x}, t)$. Let (R, θ, ϕ) be the spherical coordinates of a listening position $\boldsymbol{x}$ relative to O's center of mass. We model the pressure field at $\boldsymbol{x}$ as

$$p(\boldsymbol{x}, t) = \sum_{k=1}^{N} \frac{1}{R^k} q_k \left(\theta, \phi, t - \frac{R}{c} \right) \qquad (20)$$

for some number of terms N, where c is the speed of sound. For a fixed angular direction (θ, ϕ) we discretize the signals q_k at sampling rate $1/\Delta t$ and define

$$\{ \dots, q_k^{-2}, q_k^{-1}, q_k^0, q_k^1, q_k^2, q_k^3, \dots \} \text{ where } q_k^j = q_k(\theta, \phi, j\Delta t). \qquad (21)$$

The continuous signal q_k is computed via

$$q_k(\theta, \phi, t) = \sum_j q_k^j \psi(t - j\Delta t; \Delta t) \qquad (22)$$

where ψ is the cubic filter (17). To determine the numerical values of q_k^j, we precompute the following pressure time series

$$\{ \dots, p_i^{-2}, p_i^{-1}, p_i^0, p_i^1, p_i^2, p_i^3, \dots \} \text{ where } p_i^\ell = p(\theta, \phi, R_i, \ell\Delta t) \qquad (23)$$

for several radii $R_1, \dots, R_M$ with $M \geq N$. Then, using (20) and (22) we have

$$p_i^\ell = \sum_{k=1}^{N} \frac{1}{R_i^k} q_k \left(\theta, \phi, \ell\Delta t - \frac{R_i}{c} \right) \qquad (24)$$

$$= \sum_{k=1}^{N} \sum_j \frac{\psi \left((\ell - j)\Delta t - \frac{R_i}{c} \right)}{R_i^k} q_k^j. \qquad (25)$$

We write (25) as a system of linear equations $\mathbf{Aq} = \mathbf{p}$ and use a truncated singular value decomposition (TSVD) to find a least-squares solution. Given the values q_k^j provided by this solution, $p(\boldsymbol{x}, t) = p(\theta, \phi, R, t)$ can be evaluated for arbitrary R and t using (20) and (22). Finally, we uniformly discretize the angle space around $\boldsymbol{x}_0$ and repeat this procedure for each direction, noting that the system (25) is the same for all directions, so its SVD needs to only be computed once.

For each of our example objects we precompute $N = 2$ terms using solutions computed at $M = 5$ radii. We define $R_1 = 2R$ where R is the radius of object O's bounding sphere centered at $\boldsymbol{x}_0$. For subsequent radii, we use $R_i = \kappa^{i-1} R_1$. We choose $\kappa = 2^{1/4}$ so that $R_5 = 4R$. Outgoing directions from each object are discretized using uniform 40×80 or 5×10 discretizations of the (θ, ϕ) angle space (see §5 for discussion). We evaluate the field in arbitrary directions using linear interpolation in (θ, ϕ) angle space.
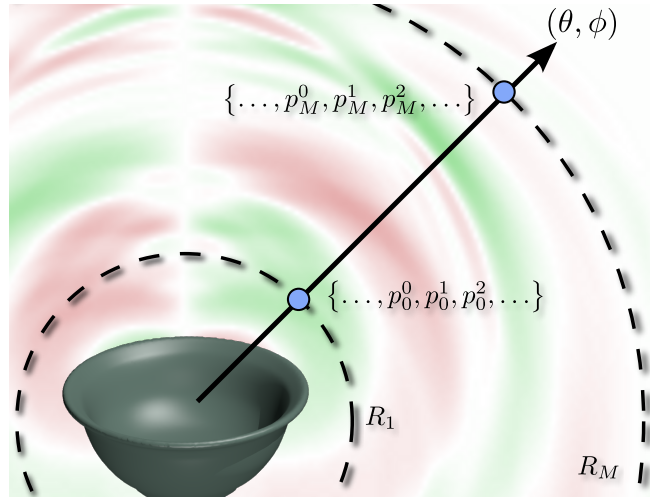

Figure 6: Precomputation Sampling Geometry: *The pressure series* (23) *are computed at radii* $R_1, \dots R_M$ *in the direction* (θ, ϕ) *via direct numerical simulation of the acoustic wave equation. The innermost and outermost radii are visualized and the points at which pressure series are evaluated are shown in blue.*

4.3 Synthesizing Rigid Acceleration Noise

We combine the time-scale estimation described in §3 with precomputed acceleration noise to efficiently synthesize rigid-body acceleration sound. The time-scale h (§4.2) is determined via a simple approach based on (7). Let m_1, ρ_1, E_1 and ν_1 be the mass, density, Young's modulus and Poisson ratio of object O. Next, let $r_1 = (0.75m_1/\rho_1)^{1/3}$; that is, the radius of the sphere whose mass and density match those of O. Using (7), we compute the time scale τ due to the collision of this sphere with another sphere of infinite radius, mass and stiffness $r_2 = m_2 = E_2 = \infty$ (effectively an infinitely stiff, infinitely massive plane) at $V = 5$m/s (roughly the speed due to a 1m fall). Finally, we set the pulse time scale for O to be $h = \tau/5$. We find that this time scale is sufficiently small to accurately approximate the acceleration pulses produced in typical rigid body collision scenarios.

Sound is evaluated using the time-series of collision impulses generated by a rigid-body solver. To avoid noise due to small impulses acting on bodies in static contact, we discard all impulses for which the relative collision velocity lies below some threshold v_{min}. In all of our examples, we used $v_{min} = 5$cm/s. We estimate a contact time scale τ for a rigid-body impulse occurring between bodies O_1 and O_2 at time t_0 with relative velocity exceeding v_{min}. As in §3.3, we make the simplifying assumption that the change in position/orientation of each body is negligible in the time period $[t_0, t_0 + \tau]$. We transform the listening position $\boldsymbol{x}$ in to each body's coordinate frame by applying the inverse rigid body transformations of O_1 and O_2 at time t_0. Finally, the pressure due to each body's acceleration is computed for these transformed positions using (18-19) with continuous acceleration signals determined by (11-12). This process is summarized in Figure 7.

5 Results

Implementation Details: Rigid-body simulations are run with a solver based on [Guendelman et al. 2003]. Modal sound dynamics are driven using the same continuous forces used to produce acceleration noise (see §3). We integrate linear modal vibration dynamics using an implicit Newmark scheme [Hughes 2000] with a time step of $\Delta t = 1/192000$s and evaluate acoustic transfer
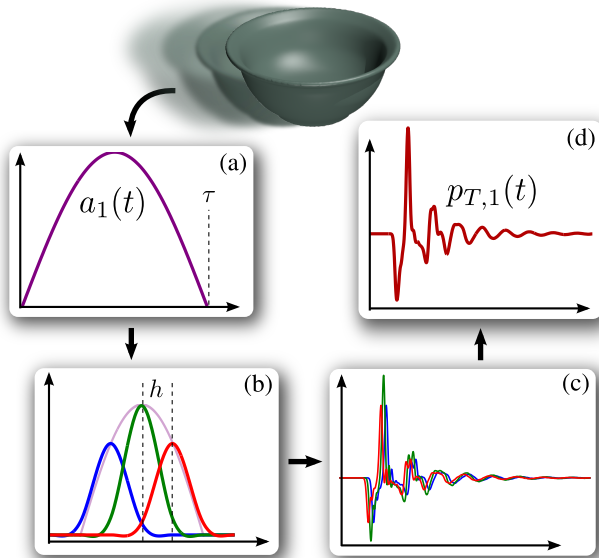
Figure 7: Approximating impulse pressure: (a) *An impulse applied to the bowl results in acceleration along the bowl's x-axis with time-profile $S(t; t_0, \tau)$;* (b) *$S(t; t_0, \tau)$ is decomposed using appropriately scaled and offset instances of $\psi(t; h)$;* (c) *the corresponding directional pulse $p_{T,1}^{(h)}$ in the direction of listening position $\boldsymbol{x}$ is computed via* (20)*, then scaled and offset according to the coefficients and offsets from part* (b)*;* (d) *the scaled and offset instances of $p_{T,1}^{(h)}$ are added together to reconstruct the full pressure signal experienced at listening position $\boldsymbol{x}$.*

due to modal vibration using the *FastBEM Acoustics* implementation (www.fastbem.com) of the fast multipole boundary element method [Liu 2009; Shen and Liu 2007]. We found the popular Rayleigh damping model to be insufficient for generating realistic results in some of our examples. We extended this model with an additional damping term proportional the inverse stiffness matrix of the linear elastic system and found that the additional control provided by this model allowed us to produce much more realistic results for certain objects. All sounds were computed at a virtual microphone position of $\boldsymbol{x} = [1.0 \ 1.8 \ 1.0]^T$. For reference, the table appearing in our examples is centered at $x = z = 0$, elevated 40cm off the ground and has length 1.8m in the x-axis and width 0.8m in the z-axis. Modal sounds are delayed according to the distance between each object's center of mass and the microphone.

The precomputed solutions (23) are evaluated with a finite difference time-domain (FDTD) wave equation solver. We use the perfectly matched layers approach from [Liu and Tao 1997] to solve the PDE on as small a domain as possible while avoiding reflections from the domain boundary. Equations (3-4) are time-stepped with a 2nd-order leapfrog scheme using a 2nd-order discretization in space via a staggered pressure/velocity grid (see [Liu and Tao 1997] for details). We carefully compared results from our solver and FastBEM with analytical wave equation solutions in [Koss and Alfredson 1973] to guarantee correct physical scaling between modal and acceleration sound.

Acceleration Noise Precomputation: Statistics for the acceleration pulse precomputation described in §4.2 are given in Table 1. In general, we find that objects with a mostly convex shape require fairly short precomputation simulations, while more concave objects tend to produce more acoustic intra-reflections and hence require longer simulation times.

EXAMPLE (Ball bearing): Our simplest example is a spherical steel ball bearing with a radius of 7.5mm. All of the vibration

modes for this object have frequencies well above the range of human hearing. As a result, modal sound synthesis produces no meaningful sound for model. By including acceleration noise, we recover the familiar clicks produced when these objects collide.

EXAMPLE (Dice): We model dice with two different shapes. As in the case of the ball bearing, all vibration frequencies for these objects are inaudible. Our approach is able to recover the familiar sound of dice rolling on a table.

EXAMPLE (Coin): For this example, we model a copper coin with roughly the same dimensions as an American quarter. While this object certainly produces significant ringing noise, the results produced by modal synthesis alone sound muffled and provide little temporal distinction between object impacts. The addition of acceleration noise allows us to recover detailed impact sounds.

EXAMPLE (Key and ring): As in the case of the coin, these objects have some audible ringing noise, but the inclusion of acceleration noise results in significantly more crisp, detailed sound.

EXAMPLE (Mug): Because the mug's shape, sustained acoustic reflections occur in its interior even for short boundary acceleration pulses. As a result, the acceleration noise for this object produces a noticeably pitched tone. To resolve this behavior we were required to run the precomputation simulation for a significantly longer time period than was sufficient for other examples. Due to the length of the signal associated with this simulation, the least-squares system (25) was very large, resulting in a costly TSVD solve.

EXAMPLE (Plate and bowl): These examples illustrate that as objects increase in size, the significance of acceleration noise relative to ringing noise diminishes. Nevertheless, the addition of acceleration noise in these examples still results in a subtle brightening of contact sounds.

EXAMPLE (Fracture): We use rigid-body fracture simulation and sound data generated by the methods of [Zheng and James 2010] to generate improved fracture sounds for animations of a breaking plate and a breaking pane of glass. Since fracture simulations tend to produce large ensembles of small objects, the absence of acceleration noise is particularly noticeable. By including acceleration noise, we produce sounds with significantly enhanced temporal detail as objects break apart and the resulting pieces collide with each other. The plate example in particular illustrates that our model is also capable of resolving other continuous sound phenomena, such as rolling motion.

Precomputed Acceleration Noise Validation: Recall that when building the pulse approximations discussed in §4.2 the largest radius at which we sample pressure values is $4R$, where R is the bounding sphere radius of the object. We run a FDTD domain simulation of the wave equation using acceleration boundary conditions of the form (11-12) and sample the pressure time series at a set of listening locations located at a radius of $8R$ (well outside of the largest radial shell used for precomputation). We compare the directly simulated result to the pressure field computed using our approach (18-19). We see that results computed with our method closely match ground truth FDTD result, with error generally manifested in the form of a small (on the order of a few samples) delay between the two signals (see Figure 8). We also note here that listening positions chosen for this evaluation were not chosen to be aligned with a direction from the discretized PAN field (see §4).

Figure 8 also compares results computed using PAN models with different angular resolutions. Due to the smoothness of acceleration noise field, we see comparable results when using PAN fields discretized at resolutions of either 40×80 or 5×10. While this distinction does not influence synthesis time, it does affect memory usage (see Table 1). In Figure 9 we compare results from PAN

Model	ρ (kg/m^3)	E (GPa)	ν	f_{min} (kHz)	Grid res.	T	h (μs)	Sim. time	Solve time	40×80 field size	5×10 field size
Ball Bearing	123.4	0.34	8940	159.5	125^3	1ms	7.3264	6m, 55s	2.7s	23.5 MB	0.42 MB
Bowl	72	0.19	2700	2.00	220^3	10ms	24.332	40m, 19s	2m, 16s	133 MB	2.15 MB
Coin	123.4	0.34	8940	10.07	215^3	2ms	4.8333	141m, 18s	3.3s	35 MB	0.6 MB
Dice	2.4	0.37	1200	32.9	170^3	1ms	14.898	17m, 38s	7.3s	35 MB	0.6 MB
Key	123.4	0.34	8940	2.03	350^3	1ms	5.56629	63m, 39s	46.4s	136 MB	2.3 MB
Key Ring	123.4	0.34	8940	3.94	245^3	1ms	5.56629	40m, 52s	5.0s	46 MB	0.8 MB
Mug	72	0.19	2700	1.32	195^3	13ms	25.467	115m, 59s	282m 1s	1131 MB	19 MB
Plate	72	0.19	2700	1.00	300^3	5ms	27.358	53m, 26s	28.1s	108 MB	1.8 MB
Rounded Dice	2.4	0.37	1200	29.2	170^3	1ms	17.469	16m, 58s	4.2s	35 MB	0.6 MB
Broken plate (11 pieces)	72	0.19	2700	Varied	Varied (4mm grid cells)	6ms	See §4.3	132m, 6s (all pieces)	3m, 17s (all pieces)	800 MB (all pieces)	14 MB (all pieces)
Broken glass pane (71 pieces)	62	0.2	2600	Varied	Varied (4mm grid cells)	2.5ms	See §4.3	13h, 12m (all pieces)	21m, 45s (all pieces)	6000 MB (all pieces)	95 MB (all pieces)

Table 1: Model and Precomputation Statistics: *The finite difference grid resolution, simulation duration (T) and pulse time scale h used to precompute the pulse approximation introduced in §4.2. Simulation times and least-squares solve times are also provided. The field size columns indicate the memory usage to store the precomputed acceleration noise model at angular resolutions of 40×80 and 5×10. Timing/memory results for the fracture examples represent the time/memory taken to precompute/store the acceleration noise model for all pieces generated in the fracture simulation. Material parameters and the lowest modal vibration frequency (f_{min}) are provided for all objects. Simulations and solves were run on 8-core Intel Xeon X5570 and X7560 machines.*

fields with different pulse time scales h (see §4). All examples involving the bowl mesh are computed with a pulse time scales of $h = h_{base} = 24.322\mu$s. The following table provides synthesis times for the "multiple bowl drop" example synthesized with different time scales:

h	h_{base}	$2h_{base}$	$4h_{base}$	$8h_{base}$
Synthesis time (s)	3.15	1.98	1.25	0.89

Larger pulse time scales result in shorter synthesis times since fewer pulses need to be included for each impact. See the accompanying result video for a comparison of sounds synthesized using all four time scales. We observe little audible difference between sounds synthesized with pulse time scales of h_{base} and $2h_{base}$, suggesting that our method is effectively interpolating impact accelerations. However, synthesis with larger time scales results in audible differences and degraded sound quality, with many high-frequency features being omitted.

Precomputed Acceleration Noise Visualization: See the supplemental result video for animations of precomputed pressure fields (23) for some of our example objects.

Directional Resolution of Precomputed Solutions: We store precomputed acceleration noise pulses at two different angular resolutions and compare their sound contributions. While we certainly observe high numerical accuracy when using a finely discretized angular resolution of 40×80, the sounds produced by a much smaller field with an angular resolution of 5×10 are nearly indistinguishable. Table 1 lists the memory usage of these two fields for all objects.

We observe that we are able to obtain high accuracy using fields discretized at substantially lower resolutions than those used for far field acoustic transfer maps in [Chadwick et al. 2009]. This is possible because precomputed acceleration noise fields tend to exhibit substantially less angular complexity than high-frequency modal transfer functions (compare, for example, Figure 4 in this work with Figures 10 and 11 in [Chadwick et al. 2009]).

Sound Synthesis Performance: Table 2 provides sound synthesis statistics for each of our examples. Synthesis times depends on the number of impulses produced by the rigid-body simulator, and the precomputed acceleration noise pulse lengths (§4.2) for each object.

Processed Results: For short transient sounds such as those produced by our method we find that the addition of environmental reverberation can produce more plausible results. We also apply dynamic range compression to certain results, since normalizing pressure time series to have unit ℓ_∞ norm tends to produce sounds

Example	Duration (s)	Δt (ms)	# impulses		Synthesis time (s)
Ball drop	5	2.5	1750916	(23411)	7.96
Coin drop	8	0.1	17307535	(22959)	16.00
Coin drop (w/ table)	8	0.1	3886215	(24045)	18.19
Dice drop (w/ plate)	5	1.0	26899	(3414)	0.88
Dice drop (w/ table)	5	1.0	44689	(683)	0.40
Key Chain	5	0.1	2052579	(48828)	12.36
Mug/Coin drop	5	1.0	383877	(3796)	2.68
Multiple bowl drop	5	1.0	23712	(1992)	3.29
Multiple mug drop	5	1.0	25147	(319)	10.33
Multiple plate drop	5	1.0	70007	(1303)	3.72
Plate fracture	5	0.025	3962503	(1293)	2.23
Glass fracture	2	0.025	11556813	(2507)	3.77

Table 2: Sound Synthesis Statistics: *Acceleration sound synthesis times (averaged over 5 trials) for our examples. The duration and Δt columns report the length and time step duration for the rigid-body simulation. # impulses refers to number of impulses produced in the simulation (bracketed numbers are the number of impulses with relative velocity exceeding v_{min} – see §4.3). Synthesis was performed on an 8-core Intel X5570 machine.*

in which some parts seem abnormally quiet. See the supplemental video for both dry and processed results for certain examples. Effects are added using *Adobe Soundbooth* during post-processing.

6 Conclusion

We presented a practical model for synthesizing rigid-body acceleration noise. Sound is computed efficiently via precomputed approximations of the pressure field due to objects undergoing short acceleration pulses. This model allows us to recover an important component of rigid-body sound not modeled by traditional modal vibration. The addition of acceleration noise significantly improves the sound quality for a variety of rigid-body examples.

Limitations and Future Work: We make a number of simplifications when estimating a continuous contact force between colliding objects. Efficient and accurate determination of continuous contact forces is a challenging open problem. Effects such as inelasticity and variation due to contact region geometry may play a role in the production of acceleration noise. Moreover, our contact force model only considers normal contact. As such, acceleration sounds due to frictional effects (e.g., a coin spinning on end, or a rolling ball) are difficult to synthesize [van den Doel et al. 2001]. Although computational methods exist to resolve these phenomena (e.g., [Hippmann 2004]), they are computationally expensive and require careful parameter tuning. Further compression of the precomputed acceleration noise model (say, by individual compression of each directional time signal) and extending our model to real-time settings are other areas interesting areas for future work.

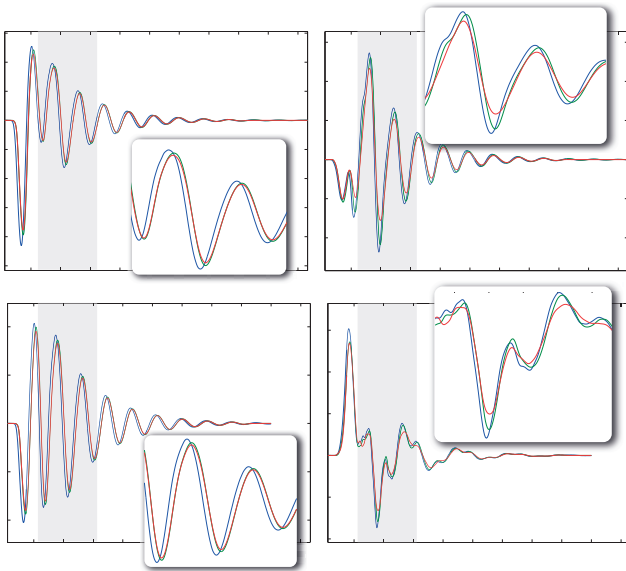Our examples demonstrate that acceleration noise makes a signifi-

Figure 8: PAN angular sampling comparison: *Pressure time series due to acceleration of a bowl mesh computed using an FDTD wave equation solver (blue), PAN discretized at angular resolution 40×80 (green) and PAN discretized at angular resolution 5×10 (red). We measure the pressure time series at two listening positions for both translational (top row) and rotational (bottom row) acceleration pulses with time profile $S(t; \tau/4, \tau)$ where $\tau = 0.0001s$. Inset figures magnify the highlighted regions of the original plots to make details more evident.*
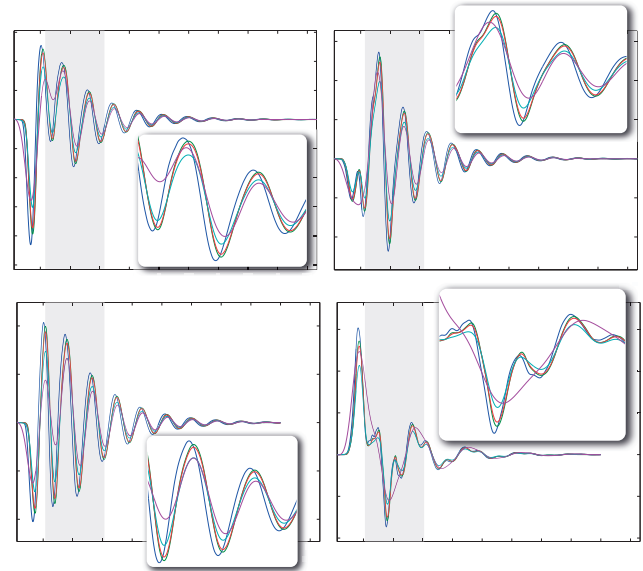

Figure 9: PAN temporal resolution comparison: *Pressure time series due to acceleration of a bowl mesh. We compare results from a FDTD solver (blue), PAN solutions computed with pulse time scale $h = h_{base} = 24.322\mu s$ (green), PAN solutions with $h = 2h_{base}$ (red), PAN with $h = 4h_{base}$ (cyan) and PAN with $h = 8h_{base}$ (magenta). We measure the pressure time series at two listening positions for both translational (top row) and rotational (bottom row) acceleration pulses with time profile $S(t; \tau/4, \tau)$ where $\tau = 0.0001s$.*

cant contribution to rigid-body fracture sounds. For these examples we explicitly precompute solutions (§4) for each fragment produced by the fracture solver. In [Zheng and James 2010], the authors use proxy object geometry to avoid explicitly constructing modal sound data for each fracture object. This model could be expanded by introducing a similar proxy object model for acceleration noise.

As has been the case in previous work on rigid-body sound synthesis, we generate results independently for each object. This may fail to capture interesting and potentially important effects. Our experiments suggest that effects such as inter-object and environmental scattering can be particularly important for short, transient sounds such as acceleration noise or sound from highly damped modal vibration. Neglecting these effects may produce results that sound somewhat harsh or abrupt in some cases. For example, the acceleration noise produced by two small metal spheres colliding is altered dramatically by the addition of environmental reverb. Efficiently resolving both inter-object and environmental acoustic scattering for physically based animations such as the ones shown in our results is a challenging open problem.

References

BONNEEL, N., DRETTAKIS, G., TSINGOS, N., VIAUD-DELMON, I., AND JAMES, D. 2008. Fast Modal Sounds with Scalable Frequency-Domain Synthesis. *ACM Transactions on Graphics 27*, 3 (Aug.), 24:1–24:9.

CHADWICK, J. N., AN, S. S., AND JAMES, D. L. 2009. Harmonic Shells: A Practical Nonlinear Sound Model for Near-Rigid Thin Shells. *ACM Transactions on Graphics (Proceedings of SIGGRAPH Asia 2009) 28*, 3 (Dec.).

CHAIGNE, A., AND LAMBOURG, C. 2001. Time-domain simulation of damped impacted plates. i. theory and experiments. *Journal of the Acoustical Society of America 109*, 4, 1422–1432.

ENDO, M., NISHI, S., NAKAGAWA, M., AND SAKATA, M. 1981. Sound radiation from a circular cylinder subjected to elastic collision by a sphere. *Journal of Sound and Vibration 75*, 2, 285–302.

FLORES, P., AMBRÓSIO, J., CLARO, J. C. P., AND LAKARANI, H. M. 2006. Influence of the contact-impact force model on the dynamic response of multi-body systems. In *Proceedings of the Institution of Mechanical Engineers. Part K: Journal of Multi-Body Dynamics*, vol. 220, 21–34.

FLORES, P., AMBROSIO, J. A. C., CLARO, J. C. P., AND LANKARANI, H. M. 2008. Springer, ch. 3: Contact-Impact Force Models for Mechanical Systems.

FLORES, P., MACHADO, M., AND SILVA, M. T. 2011. On the continuous contact force models for soft materials in multibody dynamics. *Multibody System Dynamics 25*, 3, 357–375.

GILARDI, G., AND SHARF, I. 2002. Literature survey of contact dynamics modelling. *Mechanism and Machine Theory 37*, 10, 1213–1239.

GUENDELMAN, E., BRIDSON, R., AND FEDKIW, R. 2003. Nonconvex rigid bodies with stacking. *ACM Transactions on Graphics (Proceedings of SIGGRAPH 2003) 22*, 3 (Aug.).

HERTZ, H. 1882. Über die Berührung fester elastiche Körper and über die harte (On the contact of elastic solids). *J. reine und angewandte Mathematk 92*, 156–171.

HIPPMANN, G. 2004. An algorithm for compliant contact between complexly shaped bodies. *Multibody System Dynamics 12*, 4, 345–362.

HUGHES, T. J. R. 2000. *The Finite Element Method: Linear Static and Dynamic Finite Element Analysis*, second ed. Dover Publications, Inc., Mineola, New York.

HUNT, K. H., AND CROSSLEY, F. R. E. 1975. Coefficient of restitution interpreted as damping in vibroimpact. *Journal of Applied Mechanics 42*, 2, 440–445.

JAMES, D. L., BARBIČ, J., AND PAI, D. K. 2006. Precomputed Acoustic Transfer: Output-sensitive, accurate sound generation for geometrically complex vibration sources. *ACM Transactions on Graphics 25*, 3 (July), 987–995.

JOHNSON, K. L. 1985. *Contact Mechanics*. Cambridge University Press.

KOSS, L. L., AND ALFREDSON, R. J. 1973. Transient sound radiated by spheres undergoing and elastic collision. *Journal of Sound and Vibration 27*, 1, 59–75.

LAMBOURG, C., CHAIGNE, A., AND MATIGNON, D. 2001. Time-domain simulation of damped impacted plates. ii. numerical model and results. *Journal of the Acoustical Society of America 109*, 4, 1433–1447.

LANKARANI, H. M., AND NIKRAVESH, P. E. 1990. A contact force model with hysteresis damping for impact analysis of multibody systems. *Journal of Mechanical Design 112*, 369–376.

LIU, Q.-H., AND TAO, K. 1997. The perfectly matched layer for acoustic waves in absorptive media. *Journal of the Acoustical Society of America 102*, 4, 2072–2082.

LIU, Y. J. 2009. *Fast Multipole Boundary Element Method: Theory and Applications in Engineering*. Cambridge University Press, Cambridge.

LLOYD, B., RAGHUVANSHI, N., AND GOVINDARAJU, N. K. 2011. Sound synthesis for impact sounds in video games. In *Proceedings of I3D 2011 Symposium on Interactive 3D Graphics and Games*.

MEHRABY, K., KHADEMHOSSEINI, H., AND POURSINA, M. 2011. Impact Noise Radiated by Collision of Two Spheres: Comparison Between Numerical Simulations, Experiments and Analytical Results. *Journal of Mechanical Science and Technology 25*, 7, 1675–1685.

MEYER, M., DESBRUN, M., SCHRÖDER, P., AND BARR, A. H. 2002. Discrete differential-geometry operators for triangulated 2-manifolds. *VisMath*.

MITCHELL, D. P., AND NETRAVALI, A. N. 1988. Reconstruction filters in computer-graphics. In *Proceedings of SIGGRAPH 1988*, 221–228.

O'BRIEN, J. F., COOK, P. R., AND ESSL, G. 2001. Synthesizing sounds from physically based motion. In *Proceedings of ACM SIGGRAPH 2001*, Computer Graphics Proceedings, Annual Conference Series, 529–536.

O'BRIEN, J. F., SHEN, C., AND GATCHALIAN, C. M. 2002. Synthesizing sounds from rigid-body simulations. In *ACM SIGGRAPH Symposium on Computer Animation*, 175–181.

PAPETTI, S., AVANZINI, F., AND ROCCHESSO, D. 2011. Numerical methods for a nonlinear impact model: A comparative study with closed-form corrections. *IEEE Transactions on Audio, Speech and Language Processing 19*, 7, 2146–2158.

REN, Z., YEH, H., AND LIN, M. 2010. Synthesizing contact sounds between textured models. In *Virtual Reality Conference (VR), 2010 IEEE*, 139 –146.

RICHARDS, E. J., WESCOTT, M. E., AND JAYAPALAN, R. K. 1979. On the prediction of impact noise, i: Acceleration noise. *Journal of Sound and Vibration 62*, 4, 547–575.

RICHARDS, E. J., WESCOTT, M. E., AND JAYAPALAN, R. K. 1979. On the prediction of impact noise, ii: Ringing noise. *Journal of Sound and Vibration 65*, 3, 419–451.

ROSS, A., AND OSTIGUY, G. 2007. Propagation of the initial transient noise from an impacted plate. *Journal of Sound and Vibration 301*, 1, 28–42.

SCHEDIN, S., LAMBOURGE, C., AND CHAIGNE, A. 1999. Transient sound fields from impacted plates: Comparison between numerical simulations and experiments. *Journal of Sound and Vibration 221*, 3, 471–490.

SCHIEHLEN, W., AND SEIFRIED, R. 2004. Three approaches for elastodynamic contact in multibody systems. *Multibody System Dynamics 12*, 1, 1–16.

SERRA, X., AND SMITH, J. 1990. Spectral modeling synthesis: A sound analysis/synthesis system based on a deterministic plus stochastic decomposition. *Computer Music Journal 14*, 4, 12–24.

SHEN, L., AND LIU, Y. J. 2007. An adaptive fast multipole boundary element method for three-dimensional acoustic wave problems based on the Burton-Miller formulation. *Computational Mechanics 40*, 3, 461–472.

STOELINGA, C. N. J., AND LUTFI, R. A. 2011. Modeling manner of contact in the synthesis of impact sounds for perceptual research. *Journal of the Acoustical Society of America 130*, 2, EL62–EL68.

VAN DEN DOEL, K., KRY, P. G., AND PAI, D. K. 2001. FoleyAutomatic: Physically Based Sound Effects for Interactive Simulation and Animation. In *Proceedings of ACM SIGGRAPH 2001*, Computer Graphics Proceedings, Annual Conference Series, 537–544.

VERMA, T. S., AND MENG, T. H. Y. 2000. Extending spectral modeling synthesis with transient modeling synthesis. *Computer Music Journal 24*, 2, 47–59.

WÅHLIN, A. O., GREN, P. O., AND MOLIN, N.-E. 1994. On structure borne sound: Experiments showing the initial transient acoustic wave field generated by an impacted plate. *Journal of the Acoustical Society of America 96*, 5, 2791–2797.

YUFANG, W., AND ZHONGFANG, T. 1992. Sound Radiated from the Impact of Two Cylinders. *Journal of Sound and Vibration 159*, 2, 295–303.

ZHENG, C., AND JAMES, D. L. 2010. Rigid-body fracture sound with precomputed soundbanks. *ACM Transactions on Graphics (Proceedings of SIGGRAPH 2010) 29*, 3 (July).

ZHENG, C., AND JAMES, D. L. 2011. Toward high-quality modal contact sound. *ACM Transactions on Graphics (Proceedings of SIGGRAPH 2011) 30*, 4 (Aug.).